Multi-mJ, kHz, ps deep-ultraviolet source

Chun-Lin Chang,[1] Peter Krogen,[1] Houkun Liang,[1] Gregory J. Stein,[1] Jeffrey Moses,[1] Chien-Jen Lai,[1] Jonathas P. Siqueira,[1] Luis E. Zapata,[2,3] Franz. X. Kärtner,[1,2,3] and Kyung-Han Hong,[1,*]

[1]*Department of Electrical Engineering and Computer Science and Research Laboratory of Electronics, Massachusetts Institute of Technology (MIT), Cambridge, Massachusetts 02139, USA*
[2]*Center for Free-Electron Laser Science, DESY and Department of Physics, University of Hamburg, Hamburg, Germany*
[3]*The Hamburg Center for Ultrafast Imaging, Luruper Chaussee 149, 22761 Hamburg, Germany*
**Corresponding author: kyunghan@mit.edu*

Received December 14, 2014; accepted January 07, 2015; posted Month X, 2015
(Doc. ID 230814); published Month X, 2015

We demonstrate a 0.56 GW, 1 kHz, 4.2 ps, 2.74 mJ deep-ultraviolet (DUV) laser at ~257.7 nm with a beam propagation factor (M^2) of ~2.54 from a frequency-quadrupled cryogenic multi-stage Yb-doped chirped-pulse amplifier. The frequency quadrupling is achieved using LiB_3O_5 and β-BaB_2O_4 crystals for near-infrared (NIR)-to-green and green-to-DUV conversion, respectively. An overall NIR-to-DUV efficiency of ~10% has been achieved, which is currently limited by the thermal-induced phase mismatching and the DUV-induced degradation of transmittance. To the best of our knowledge, this is the highest-peak-power picosecond DUV source from a diode-pumped solid-state laser operating at kHz repetition rates.

OCIS Codes: (140.3610) Lasers, ultraviolet; (190.2620) Harmonic generation and mixing; (140.3615) Laser, ytterbium; (140.7090) Ultrafast lasers.
http://dx.doi.org/10.1364/OL.99.099999

High-power deep-ultraviolet (DUV, λ < 300 nm) lasers have various scientific, industrial, and medical applications, such as photo-cathodes for accelerator facilities [1], spectroscopy, photolithography, precise micromachining, and ophthalmology. Apart from excimer lasers, ultrafast diode-pumped solid-state lasers (DPSSLs) capable of efficient nonlinear frequency conversion are suited for practical applications in those areas.

Wavelengths in the DUV range have significant advantages over the ~355 nm traditionally used for micromachining, owing to its high spatial resolution, high absorption and ability to break stronger atomic bonds [2]. Furthermore, for a pulse duration shorter than the time scales of electron diffusion and lattice heating, which is typically ~10 ps [3], a heat-affected zone with melt and evaporation can be significantly reduced. In addition, the fluence of surface damage threshold is at minimum. In this unique parameter space, *i.e.*, sub-10 ps DUV, scaling up the pulse energy beyond one millijoule (mJ) at high repetition rates can significantly be advantageous for high-precision, high-volume manufacturing processes based on cold ablations that ensure a stable ablation threshold regardless of material impurity due to high absorption.

On the other hand, ultrafast pump sources that deliver high energy pulses at high repetition rates are also extremely important for energy and power scaling of optical parametric amplification (OPA) and optical parametric chirped-pulse amplification (OPCPA). Using a DUV pump source enables to extension of the OPA/OPCPA output spectra into the UV range [4]. A pump duration in the ps time scale is considered as an excellent compromise for signal pulses short enough to allow for stretching and compression while handling high energies for ultrabroadband OPCPA systems [5]. Furthermore, the frequency conversion of the pump pulses enables to pump multi-stage OPCPAs in multi-colors, covering a full octave of bandwidth [6] and eventually realizing multi-octave energy scalable pulse synthesizers [7].

So far, there has still not been a commercial ps DUV DPSSL product capable of providing a mJ-level output with a <10-ps duration at kHz repetition rates. Recently, a powerful DUV ps laser was reported which generated with a peak power of >megawatt (MW) level [8] at 1 kHz. A multi-MW output was also reported with a pulse energy close to one mJ, but suffered from low repetition rates [9]. Besides the advantage of high conversion efficiency, using a powerful ps DPSSL with an excellent beam quality is a straightforward way of scaling up the average power of such an intense DUV ps laser. The high-power ps DPSSLs based on cryogenically-cooled Yb:YAG medium [10] can serve as an excellent fundamental source at ~1 μm for frequency conversion. Using this technology, we have demonstrated a green ps laser source with record-high average power by frequency doubling [11] and a 2.1-μm femtosecond laser source with multi-mJ energy by pumping OPCPAs [12]. In this Letter, we demonstrate a 2.74 mJ, 4.2 ps, 1 kHz DUV ps laser at ~257.7 nm based on a frequency-quadrupled cryogenic ultrafast Yb-doped DPSSL system in chirped-pulse amplification (CPA). The DUV peak power is 0.56 GW with a beam propagation factor of M^2<3, which easily ionizes air with less than one-tenth of the full output energy. To the best of our knowledge, this is the most intense DUV generation from a kHz DPSSL source.

Figure 1 illustrates the fundamental frequency source which is a sub-10 ps, near-IR (NIR) Yb-doped CPA laser system. It was upgraded from a high-energy pump source of our 2.1-μm OPCPA laser system [12]. An octave-spanning Ti:sapphire oscillator (Octavius-85M, IdestaQE) provides the seed source at 1030 nm, shared with an OPCPA-based synthesizer for optical synchronization. The 1030 nm pulses are successively pre-amplified to ~0.5 nJ in a four-stage single-mode Yb-doped fiber amplifier (YDFA) for seeding a regenerative amplifier (RGA). The

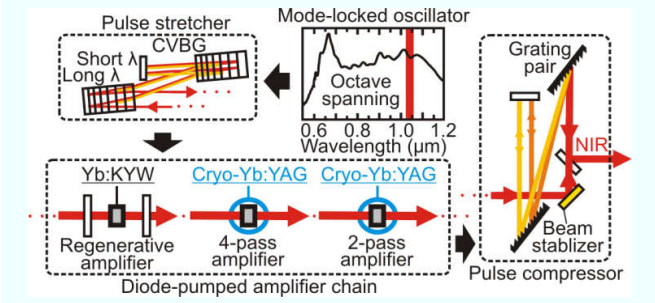

Fig. 1. Experimental layout of diode-pumped picosecond cryogenic Yb-doped laser system based on chirped-pulsed amplification. CVBG: chirped volume Bragg grating.

CPA scheme was achieved using a chirped volume Bragg grating (CVBG) pair as a stretcher and a multilayer dielectric grating pair as a compressor. More details can be found in our previous work [13]. A pulse picker based on a Pockels cell is used to reduce the repetition rate from 85 MHz to 1 kHz while suppressing the amplification of multiple pulses in the RGA.

There are three amplifier stages in the Yb-doped CPA chain. The first stage is a room-temperature Yb:KYW RGA (S-pulse HP², Amplitude Systémes) that provides a bandwidth larger than that of a cryogenic Yb:YAG RGA [14]. The second and third stage is a cryogenic Yb:YAG four-pass and two-pass amplifier, respectively. The Yb:YAG crystals are gain media for both stages and are exactly the same as that in our previous report [12]. The pulse energy from the output of the amplifier chain is 58.5 mJ for a total pump power of ~368 W with an overall energy gain of 80.7 dB and an overall efficiency of 15.9%.

The NIR spectrum measured from the output of the amplifier chain is shown in the right part of Fig. 2 (a). The full width at half maximum (FWHM) spectral bandwidth centered at 1030.6 nm is 0.34 nm which is ~1.7 times the bandwidth achieved with a cryogenic Yb:YAG RGA. It is noted that the center wavelength is offset by ~1.6 nm from that in the previous report (~1029.0 nm) [13] due to the measurement with an uncalibrated optical spectrum analyzer (OSA).

After pulse compression with a throughput of 80%, the temporal profile was measured using an autocorrelator (*pulse*Check 50, APE GmbH) as shown in Fig. 2 (b). The duration of autocorrelation in FWHM was determined to be 11.8 ps with a Gaussian fit, corresponding to a compressed pulse duration of 8.4 ps in FWHM, which is 1.6 times the transform limit. The collimated beam profile out of the compressor is presented in the inset of Fig. 2 (a). The NIR $1/e^2$ beam diameter is 5.89 mm × 5.94 mm along horizontal (x) and vertical (y) axis, respectively. A beam pointing stabilizer is installed in the compressor to reduce short-term beam pointing fluctuations as shown in Fig. 1.

Figure 3 shows the optical layout of the second harmonic generation (SHG) and the fourth harmonic generation (FHG) modules. Two subsequent stages of SHG were used to achieve frequency quadrupling. Due to the sufficiently high peak power of the NIR pulses with ~5.6 GW at maximum, a collimated input beam is used for nonlinear frequency conversion without a focusing geometry. For thermally stable operation of the amplifier chain, the NIR energy input to the SHG setup is adjusted using a half waveplate and a thin film polarizer as an energy tuner while the amplifier is operated at a full power. A lens pair Galilean telescope is used to optimize the beam size projected on the SHG crystal. The residual NIR laser pulses are completely removed using two NIR/green dichroic mirrors before the FHG setup.

Among commercial nonlinear crystals for the SHG of NIR pulses, LiB_3O_5 (LBO) is known to have the highest damage threshold (40 J/cm² at 1 ns and 18.9 GW/cm² at 1.3 ns [15]). Anti-reflection (AR) coatings for NIR and green moderately reduce the damage threshold by ~20%. We used non-critically phase-matched (NCPM) SHG with

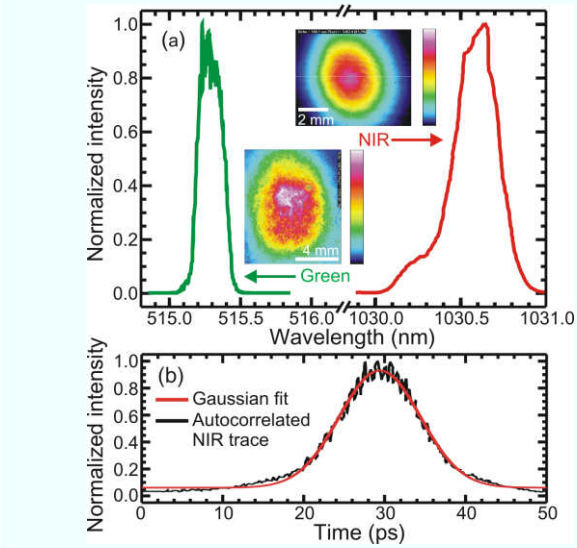

Fig. 2. (a) The normalized NIR spectrum in red and frequency-doubled spectrum in green with a measured resolution of 0.05 nm, and (b) the autocorrelation trace of the compressed NIR output. The insets in (a) show the collimated near-field images of the compressed NIR beam and the SHG green output.

an LBO crystal cut at θ=90° and φ=0° and a temperature of ~190 °C to mitigate the influence of pointing stability. The crystal dimensions are 12×12 mm² in cross-section and 15 mm in length. The spectrum of the frequency-doubled pulses is shown on the left side of Fig. 2 (a). The FWHM bandwidth centered at 515.3 nm is meaused to be 0.19 nm. The collimated green near-field image at the FHG input is shown in the inset of Fig. 2(a), where the

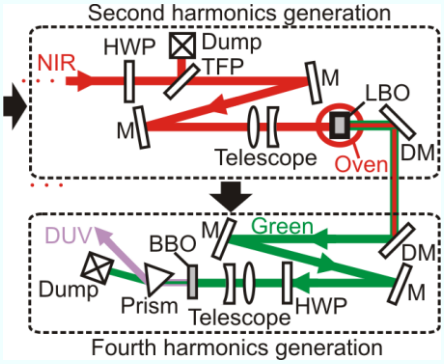

Fig. 3. Optical layout of the second harmonics generation and the fourth harmonics generation. M: Mirror; DM: Dichroic mirror; HWP: half wave plate; TFP: thin film polarizer.

beam diameter in $1/e^2$ is 9 mm × 10.4 mm along the x and y axis, respectively.

The beam propagation factor in the far field was measured using a charge-coupled device (CCD) and a plano-convex lens with f=100 cm. In Fig. 4 (a) and (b) with the fitting curve, the values of M_x^2 and M_y^2 are determined to be 1.13 and 1.21 for the NIR beam, and 1.49 and 1.89 for the green beam, which is only by 1.3–1.6 times larger. For holding the advantage of spatial precision in term of focusing quality after the frequency conversion, the degradation of beam propagation factor within 2 times with SHG is acceptable. Figure 4 (c) and (d) show the images of the focal spot profile with two dimensional outlines for NIR and green in Fig. 5 (a) and (b), respectively. Both far-field images indicate Gaussian profiles with a spot diameter in $1/e^2$ of 251 μm (x) × 267 μm (y) for NIR and 108 μm (x) × 119 μm (y) for green.

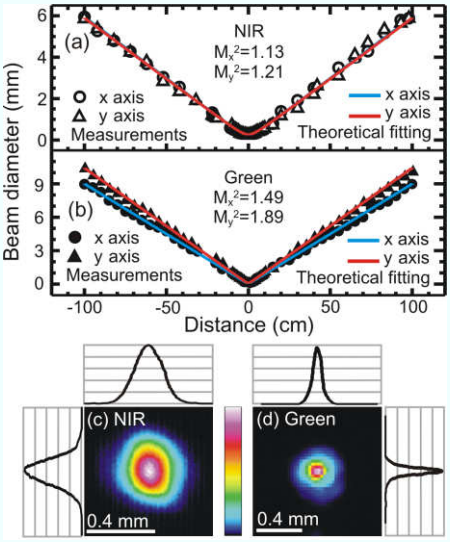

Fig. 4. The beam propagation factor measured from (a) the compressor output, and (b) the second harmonics generation with the related theoretical fittings; (c) and (d) are the measured focal spot images and 2D outlines corresponding to (a) and (b).

For optimized SHG as shown in Fig. 5 (a), a maximum green energy of ~13 mJ with a slope efficiency of 43% was achieved. As the temperature of the crystal oven (LASING BEAM) is optimized to be 189.3°C, the maximum peak power of the green pulses is up to 2.2 GW with an estimated pulse duration of ~5.9 ps and an SHG conversion efficiency is 42%. The $1/e^2$ diameter of the collimated NIR beam projected on the LBO crystal is ~11.8 mm, indicating that we fully use the entirety of the LBO crystal aperture.

The conversion efficiency starts to saturate significantly when the input NIR energy approaches 5 mJ, which corresponds to a peak power of ~0.54 GW and a $1/e^2$ peak intensity of 0.52 GW/cm². Back conversion and self-phase modulation significantly decrease the green beam size when the NIR input energy is further increased to >31.5 mJ. It implies that an LBO crystal with a larger cross section and a shorter length would be necessary for further increasing the output energy of the green pulses.

Regarding the FHG setup for DUV generation in Fig. 3, two crystals, β-BaB_2O_4 (BBO) and $CsLiB_6O_{10}$ (CLBO) [8], have shown high efficiencies. However, CLBO is highly hydroscopic and also subject to micro-cracks, making it less practical than BBO. Therefore, we selected a BBO crystal, and its nonlinear coefficient is ~1.7 pm/V and its damage threshold for green is 10 J/cm² (1 ns) and 7 GW/cm² (0.25 ps). Despite the large walk-off angle (85.13 mrad) and small crystal angle tolerance (0.18 mrad-cm) of BBO [15], a high-energy collimated beam passing through the BBO greatly relieves the effects from walk-off and angle misalignment. Due to the formation of an absorption center, the DUV-induced degradation of BBO transmittance occurs at high DUV peak power density [16]. We have selected a relatively thin crystal with a thickness of 0.5 mm and a cross section of 10×10 mm² to minimize the two-photon absorption of DUV instead of heating up the crystal. The crystal is cut for type I SHG of green at θ=48° and φ=90° and not AR-coated to avoid a significant reduction in the damage threshold for the green. A fused-silica prism is used right after the BBO crystal for separation of the residual green beam and the DUV characterization. We confirmed the DUV generation at ~258 nm by checking the refraction angle from the prism even though a DUV spectrometer was not available.

Figure 5 (b) shows that the maximum DUV energy and peak power is around 2.74 mJ and 0.56 GW, respectively. A telescope was used to optimize the green beam size and the magnification of 0.6 was found experimentally to optimize the UV conversion efficiency. When the input green energy reaches near 8 mJ, which corresponds to a peak power of ~1.35 GW or a $1/e^2$ peak intensity of 1.8 GW/cm² for the collimated green beam projected on the BBO with a $1/e^2$ diameter of ~5.8 mm, the conversion efficiency starts to saturate and reaches up to ~23%. The duration of DUV pulses and the spectral bandwidth were estimated to be ~4.2 ps and ~0.1 nm, respectively. By

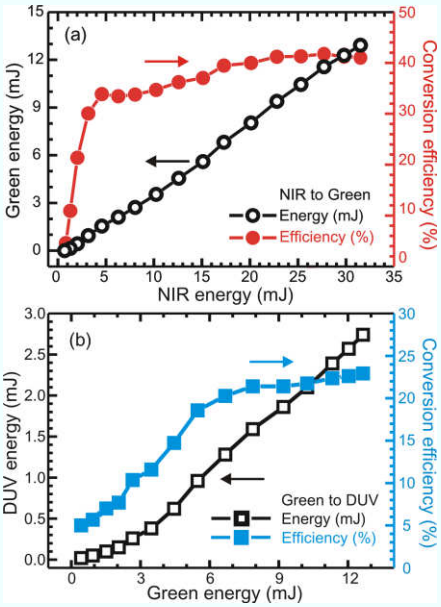

Fig. 5. Output energy and corresponding conversion efficiency of SHG at various input energies for the conversion from (a) NIR to green, and (b) green to DUV.

focusing the output beam with f/10, we are able to easily observe a spark in air by breakdown with an estimated threshold of ~10^{14} W/cm^2 by naked eye with less than one tenth of the full DUV energy. The measured beam propagation factor and the peak intensity are also consistent with the air-breakdown threshold related to NIR and green parameters.

Two-photon absorption at a high DUV peak power induces temporary defects on the crystal, but they can decay between subsequent pulses [17] at 1 kHz. Although the decay rate can be increased by heating the BBO crystal, the DUV output energy is not sensitive to crystal temperature [16], especially for a thin crystal. The temperature stabilization of the crystal can still help to increase the energy stability of DUV outputs. The overall NIR-to-DUV conversion efficiency is 9.7% with a SHG efficiency of 42%, limited by the current LBO crystal dimension, and a FHG efficiency of 23%, which is limited by the phase mismatching owing to the thermal gradient, the DUV-induced degradation of transmittance, and the aperture of the BBO crystal used.

Figure 6 (a) shows the near-field DUV beam profile with 1/e^2 diameters of 2.8 mm (x) and 4.5 mm (y) at 2 mJ. A flattop profile is observed, which is consistent with the saturation of the efficiency in Fig. 5 (b). The far-field image at the focus using an f=100 cm lens is shown in Fig. 6 (b), where the 1/e^2 diameter is 233 μm (x) and 224 μm (y), respectively. The beam is estimated by following the beam propagation and fitting as a Gaussian beam with M_x^2=1.99 and M_y^2=3.08 with an average of 2.54, which is an increase of 1.3–1.6 times from the green.

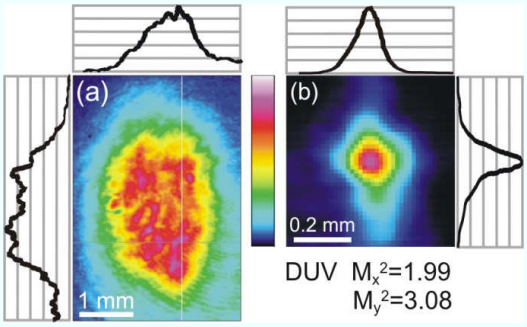

Fig. 6. With the 2D outlines, (a) the near-field DUV beam profile measured after the fused silica prism in Fig. 3, and (b) the corresponding far-field image at the focal spot. The DUV beam propagation factor measured along each axis is indicated below.

In conclusion, we demonstrated a record-high peak power of 0.5 GW, multi-mJ, kHz ~4.2 ps DUV laser with a beam propagation factor, M^2 of ~2.54 and a NIR-to-DUV conversion efficiency of ~10% from a frequency-quadrupled cryogenic Yb-doped DPSSL CPA system. This DUV source is suitable for enhanced cold-ablation in high volume manufactureing and pumping of OPCPAs.

This work was supported by AFOSR (FA9550-12-1-0499, FA9550-12-1-0080, FA9550-13-1-0159, and FA9550-14-1-0255), the Center for Free-Electron Laser Science, DESY, Germany, and the excellence cluster "The Hamburg Centre for Ultrafast Imaging—Structure, Dynamics and Control of Matter at the Atomic Scale" of the Deutsche Forschungsgemeinschaft. C.-L. Chang acknowledges the Ministry of Science and Technology in Taiwan for the Postdoctoral Research Abroad Program NSC 102-2917-I-564-026. H. K. Liang acknowledges financial support from Singapore Institute of Manufacturing Technology (SIMT/14-110023) and Agency for Science, Technology and Research (A*STAR), Singapore.

References

1. I. Will, H. I. Templin, S. Schreiber, and W. Sandner, Opt. Express **19**, 23770 (2011).
2. G. Račiukaitis, M. Brikas, M. Gedvilas, and G. Darčianovasl, J. Laser Micro. Nanoen. **2**, 1 (2007).
3. D. Du, X. Liu, G. Kom, J. Squier, and G. Mourou, Appl. Phys. Lett. **64**, 3071 (1994).
4. Gábor Kurdi, Károly Osvay, Márta Csatári, Ian N. Ross, and József Klebniczki, "Optical Parametric Amplification of Femtosecond Ultraviolet Laser Pulses," IEEE J. Sel. Topics Quantum Electron. **10**, 1259 (2004).
5. C. P. Hauri, P. Schlup, G. Arisholm, J. Biegert, and U. Keller, Opt. Lett. **29**, 1369 (2004).
6. D. Herrmann, C. Homann, R. Tautz, M. Scharrer, P. St. J. Russell, F. Krausz, L. Vetsz, and E. Riedle, Opt. Express **18**, 18752 (2010).
7. S.-W. Huang, G. Cirmi, J. Moses, K.-H. Hong, S. Bhardwaj, J. R. Birge, L.-J. Chen, E. Li, B. J. Eggleton, G. Cerullo, and F. X. Kärtner, Nature Photon. **5**, 475 (2011).
8. L. Deyra, I. Martial, F. Balembois, J. Diderjean, P. Georges, Appl. Phys. B **111**, 573 (2013).
9. L. R. Bhandari, T. Taira, A. Miyamoto, Y. Furukawa, and T. Tago, Opt. Mater. Express **2**, 907 (2012).T. Y. Fan, D. J. Ripin, R. L. Aggarwal, J. R. Ochoa, B. Chann, M. Tilleman, and J. Spitzberg, IEEE J. Sel. Top. Quantum Electron. **13**, 448 (2007).
10. T. Y. Fan, D. J. Ripin, R. L. Aggarwal, J. R. Ochoa, B. Chann, M. Tilleman, and J. Spitzberg, IEEE J. Sel. Top. Quantum Electron. **13**, 448 (2007).
11. K.-H. Hong, C.-J. Lai, A. Siddiqui, and F. X. Kärtner, Opt. Express **17**, 16911 (2009).
12. K.-H. Hong, C.-J. Lai, J. P. Siqueira, P. Krogen, J. Moses, C.-L. Chang, G. J. Stein, L. E. Zapata, and F. X. Kärtner, Opt. Lett. **39**, 3145 (2014).
13. K.-H. Hong, S.-W. Huang, J. Moses, X. Fu, C.-J. Lai, G. Cirmi, A. Sell, E. Granados, P. Keathley, and F. X. Kärtner, Opt. Express **19**, 15538 (2011).
14. K.-H. Hong, J. Gopinath, D. Rand, A. Siddiqui, S.-W. Huang, E. Li, B. Eggleton, J. Hybl, T. Y. Fan, and F. X. Kärtner, Opt. Lett. **35**, 1752 (2010).
15. SNLO software: see the website http://www.as-photonics.com/snlo
16. K. Takachiho, M. Yoshimura, Y. Takahashi, M. Imade, T. Sasaki, Y. Mori, Opt. Mater. Express **4**, 559 (2014).
17. M. Takahashi, A. Osada, A. Dergachev, P. F. Moulton, M. Cadatal-Raduban, T. Shimizu, and N. Sarukura, Jpn. J. Appl. Phys. **49**, 080211 (2010).